Control of Periodically Waked Wind Turbines

van Vondelen, Aemilius A.W.; Pamososuryo, Atindriyo K.; Navalkar, Sachin T.; van Wingerden, Jan Willem

DOI
10.1109/TCST.2024.3508577

Publication date
2025

Document Version
Final published version

Published in
IEEE Transactions on Control Systems Technology

Control of Periodically Waked Wind Turbines

Aemilius A. W. van Vondelen, Atindriyo K. Pamososuryo, Sachin T. Navalkar, and Jan-Willem van Wingerden, *Senior Member, IEEE*

***Abstract*— Periodic wakes are created on upstream wind turbines by pitching strategies, such as the Helix approach, to enhance wake mixing and thereby increase power production for wind turbines directly in their wake. Consequently, a cyclic load is not only generated on the actuating turbine's blades but also on the waked wind turbine. While the upstream load is the result of the pitching required for wake mixing, the downstream load originates from interaction with the periodic wake and only causes fatigue damage. This study proposes two novel individual pitch control schemes in which such a periodic load on the downstream turbine can be treated: by attenuation or amplification. The former method improves the fatigue life of the downstream turbine, whereas the latter enhances wake mixing further downstream by exploiting the already-present periodic content in the wake; both were validated on a three-turbine wind farm in high-fidelity large-eddy simulations. Fatigue damage reductions of around 10% were found in the load mitigation case, while an additional power enhancement of 6% was generated on the third turbine when implementing the amplification strategy. Both objectives can easily be toggled depending on a wind farm operator's demands and the desired loads/energy capture tradeoff.**

***Index Terms*— Downstream wind turbine, helix, individual pitch control, large-eddy simulation, synchronization, wake mixing.**

I. Introduction

REDUCING the cost of wind energy motivates the establishment of wind farms that profit from shared infrastructure, installation, and maintenance costs. Typically, a minimum spacing of 4–5 rotor diameters is maintained, balancing the benefits of shared costs against reduced farm-level energy production as a result of the wake effect. This event—a phenomenon occurring when upstream and downstream wind turbines align with the wind direction—causes reduced production due to lower wind speed and increased loading from wake impingement [1].

The wake effect can lead to substantial power loss, estimated at up to 20%, or an equivalent increase in loads depending on the wind farm layout [2]. Several solutions for the wake effect have been proposed in the past, such as the axial induction control method [3], which derates upstream turbines to leave more energy in the wake for downstream turbines. Studies, however, have shown that the production increase is negligible, making them more suitable for load balancing within wind farms, rather than overall production optimization [4].

A more promising remedy is wake steering, which commands a yaw misalignment in the upstream wind turbine to reposition its wake [5]. In this approach, a steady-state optimum is found, balancing the performance loss as a result of the misalignment with the performance gain obtained by alleviating turbines downstream of the wake. Since the wake is only repositioned, it might still affect other turbines further downstream.

A different approach is suggested by [6], where the wake is reduced by promoting wake mixing through dynamic variation of the induction, a method known as dynamic induction control. One implementation of this method is done by pitching periodically, hence creating a periodic structure in the wake [7]. Significant power gains are found in a two-turbine case; however, significant load increases due to thrust force variations are also shown [8].

Frederik et al. [9] propose a similar periodic actuation method that, instead of varying the thrust force's magnitude, rotates the direction around its nominal direction, significantly reducing the strong tower loads and varying power production while achieving even better performance. The helix approach, as it is colloquially called, has since garnered attention in the literature, as extensive large-eddy simulations (LESs) [10] and wind tunnel studies [11] have been performed, with multisine variations to the baseline helix also proposed [12]; all with promising results in terms of power gains.

Up until recently, little attention was given to control of the turbine in the helix wake downstream, while it poses interesting questions. First, the periodic loading as a result of the helix actuation on the upstream turbine can similarly be found on the downstream turbine. Korb et al. [13] show that applying the helix with a specific phase shift on the downstream turbine yields an additional power gain on the third turbine. They, however, do not propose a method for attaining this phase difference in control action. van Vondelen et al. [14] suggest a phase synchronization method, which can track the phase of the helix wake while similarly applying a control action downstream. However, in this method, the quality of the phase estimate depends strongly on the quality of the linear model, which changes for each operating case. It may, therefore, be challenging to obtain exact phase estimates.

The above-mentioned studies investigate the control of a downstream turbine from a power optimization perspective,

Received 12 August 2024; accepted 26 October 2024. Date of publication 13 December 2024; date of current version 25 February 2025. This work was supported in part by CrossWind C. V. and in part by Siemens Gamesa Renewable Energy. Recommended by Associate Editor C. Vermillion. *(Corresponding author: Aemilius A. W. van Vondelen.)*

Aemilius A. W. van Vondelen, Atindriyo K. Pamososuryo, and Jan-Willem van Wingerden are with the Delft Center for Systems and Control, Delft University of Technology, 2628 CD Delft, The Netherlands (e-mail: a.a.w.vanvondelen@tudelft.nl; a.k.pamososuryo@tudelft.nl; j.w.vanwingerden@tudelft.nl).

Sachin T. Navalkar is with Siemens Gamesa Renewable Energy, 2595 BN The Hague, The Netherlands (e-mail: sachin.navalkar@siemensgamesa.com).

Digital Object Identifier 10.1109/TCST.2024.3508577

while the periodic load could also be mitigated to improve fatigue life. A wind farm developer's objective is often to minimize the levelized cost of energy (LCOE) over the lifetime of the system. This is a particularly useful metric as it considers both operation and maintenance costs (which are directly related to fatigue damage) and the average power generation of the system. In our work, load mitigation and power amplification are considered as separate objectives to provide flexibility in addressing different operational goals. Load mitigation is essential for reducing fatigue damage and maintenance costs, thereby extending the turbine's lifespan. On the other hand, power amplification focuses on maximizing immediate energy capture, which is crucial for improving the overall efficiency of the wind farm. By separating these objectives, operators can tailor the control strategy to the specific needs and conditions of the wind farm, optimizing for either long-term durability or short-term performance as required. This study proposes a controller that can achieve both while relieving the control engineer from deriving a linear model for each operating case. The contributions are, hence, as follows.

1) Derivation of a novel control scheme for control of periodically waked wind turbines which can achieve the following.
   a) Load rejection through regulation.
   b) Power enhancement through synchronization by reference tracking.
2) Evaluation of 1) in a three-turbine large-eddy simulation.

The remainder of this article is organized as follows. Section II introduces the conventional individual pitch control and the helix, after which Section III presents the main contributions: the derivation of the novel control schemes. The controllers corresponding to these schemes are tuned based on an identified model in Section IV. Section V presents the simulation setup and test cases. The results of each control objective are treated in separate sections. Section VI presents the results obtained after evaluating the proposed control scheme in LES for the load mitigation objectives, while Section VII analyzes results for the synchronized wake mixing objective. Finally, conclusions are drawn in Section VIII.

II. Individual Pitch Control and the Helix

In this section, a brief introduction is given to individual pitch control for load reduction and the helix approach for wake mixing (i.e., power enhancement), which is essential background information for understanding the proposed methods. These approaches both leverage the so-called multiblade coordinate (MBC) transformation, which is used to map the pitch control system from the *rotating coordinate frame* to the *fixed coordinate frame*. This methodology is exploited in this work to derive a novel coordinate transformation, which is used to map the pitch control system from the rotating coordinate frame to the *helix coordinate frame*. As such, a considerable simplification of the pitch control system is obtained, allowing for the derivation of a novel feedback controller for: 1) load regulation and 2) phase synchronization for power enhancement, both in this section.

A. Conventional Individual Pitch Control

Significant challenges arise when larger rotors are used for wind turbines, which originate primarily from the increasing asymmetric loads caused by the spatiotemporal variability of the wind. Turbulence, wind shear, and tower shadow are amongst several phenomena that contribute to asymmetric loading, which acts on blades as they traverse through this varying wind field at the rotational frequency (once-per-revolution/1P), and its higher harmonics (2P, 3P, and so on). On the fixed structure, this loading propagates from the rotating system as a steady-state load at 0P and periodic loading at 3P, 6P, and higher in the case of a three-bladed turbine, as considered in this study.

As these loadings shorten fatigue life and structural reinforcements are costly, individual pitch control for load reduction was proposed as a solution [15]. This feedback controller exploits the MBC transformation, which maps the blade root out-of-plane moment signals M_i, $i = 1, 2, 3$, for a three-bladed wind turbine in the rotating blade coordinate frame to the fixed (nonrotating) coordinate frame, where they are collective, tilt, and yaw moments (M_{col}, M_{tilt}, and M_{yaw}, respectively), a process known as *demodulation* (e.g., [16])

$$\begin{bmatrix} M_{\text{col}} \\ M_{\text{tilt}} \\ M_{\text{yaw}} \end{bmatrix} = \underbrace{\frac{2}{3}\begin{bmatrix} 1/2 & 1/2 & 1/2 \\ \cos(\psi_1) & \cos(\psi_2) & \cos(\psi_3) \\ \sin(\psi_1) & \sin(\psi_2) & \sin(\psi_3) \end{bmatrix}}_{T_{\text{cm}}(\psi(t)=\omega_r t)} \begin{bmatrix} M_1 \\ M_2 \\ M_3 \end{bmatrix} \tag{1}$$

where ψ_i is the azimuthal position of the blades and ω_r is the rotor velocity. Note that ω_r is taken constant here and through the remainder of this article for ease of implementation and analyses. Although this is valid for low wind speed variations, the final formulation of the derivations of the main contributions will all depend on the time-dependent azimuth and can, therefore, be used with time-varying rotor speeds.

In this fixed coordinate frame, the individual pitch commands β_i can now be computed as decoupled collective, tilt, and yaw pitch commands (β_{col}, β_{tilt}, and β_{yaw}, respectively), allowing simple single-input single-output (SISO) control loops instead of more complex multiple-input multiple-output (MIMO) control. The 1P blade loading is demodulated here to the dc gain, or 0P frequency, where it is a simple bias that can easily be driven toward zero using integrator control, simplifying the pitch coordinate system significantly. In case of load imbalance, i.e., $M_1 \neq M_2 \neq M_3$, the 1P load is also demodulated to the 2P frequency [17].

Ultimately, the determined tilt and yaw commands are then mapped back to the individual blade rotating coordinate frame into pitch commands using the reverse transformation to *remodulate* the signal back into the original coordinate frame

$$\begin{bmatrix} \beta_1 \\ \beta_2 \\ \beta_3 \end{bmatrix} = \underbrace{\begin{bmatrix} 1 & \cos(\psi_1 + \psi_{\text{off}}) & \sin(\psi_1 + \psi_{\text{off}}) \\ 1 & \cos(\psi_2 + \psi_{\text{off}}) & \sin(\psi_2 + \psi_{\text{off}}) \\ 1 & \cos(\psi_3 + \psi_{\text{off}}) & \sin(\psi_3 + \psi_{\text{off}}) \end{bmatrix}}_{T_{\text{cm}}^{-1}(\psi(t)+\psi_{\text{off}})} \begin{bmatrix} \beta_{\text{col}} \\ \beta_{\text{tilt}} \\ \beta_{\text{yaw}} \end{bmatrix} \tag{2}$$

where ψ_{off} is an azimuth offset accounting for unmodeled actuator delays and blade flexibility, which is required to fully decouple the tilt and yaw channels [18].

The principle of modulation–demodulation is not only well-studied for communication networks but also sees several implementations in wind turbine control, of which individual pitch control using the MBC transform is the most famous example. Other implementations include tower side-side damping control [19], and in this work, the same principle will be applied in Section III to the frequency of the periodic load of the helix.

B. Helix Approach

The helix approach is an open-loop control strategy for power enhancement utilizing the MBC transformation to excite the blades with periodic tilt and yaw signals. These signals are determined by setting an amplitude and a frequency, where the latter parameter is governed by the dimensionless Strouhal number

$$S_{\mathrm{t}} = \frac{f_e D}{U_\infty} \tag{3}$$

where f_e is the excitation frequency of the tilt and yaw commands, D is the rotor diameter, and U_∞ is the free stream wind velocity. Strouhal values are generally selected between 0.2 and 0.4 as recommended by previous work [6], [9]. This leads to the following tilt and yaw pitch commands for helix wake mixing:

$$\begin{bmatrix} \beta_{\mathrm{tilt}} \\ \beta_{\mathrm{yaw}} \end{bmatrix} = \begin{bmatrix} A\sin(\omega_e t) \\ A\sin(\omega_e t \pm \pi/2) \end{bmatrix} \tag{4}$$

where A is the amplitude, usually no larger than 6° due to practical constraints, such as pitch rate limitations, and $\omega_e = f_e 2\pi$. Note that the collective pitch β_{col} is omitted in (4) since it is controlled by the collective pitch controller. Collective pitch control optimizes wind turbine performance by simultaneously adjusting the pitch angle of all blades based on rotor speed feedback to maintain consistent power output and rotor speed. This strategy effectively adapts to changing wind conditions, ensuring stability and protection from excessive loads.

Two helix variants exist, where setting $+\pi/2$ in β_{yaw} yields a clockwise (CW) and $-\pi/2$ a counterclockwise (CCW) rotating helix. The actuation frequency in the fixed frame remains the same for both variants. However, the actual frequency applied by the pitch actuator differs once these tilt and yaw control commands are mapped to the rotating frame

$$\beta_i = \beta_{\mathrm{col}} + \cos(\psi_i)\beta_{\mathrm{tilt}} + \sin(\psi_i)\beta_{\mathrm{yaw}} \tag{5}$$

which yields that the helix frequency in the rotating frame is at the rotation frequency ω_r plus or minus the excitation frequency ω_e (or $1P \pm f_e$), depending on CW or CCW

$$\begin{aligned} \beta_i &= \beta_{\mathrm{col}} + A\cos\left(\omega_r t + \psi_i^0\right)\beta_{\mathrm{tilt}} + A\sin\left(\omega_r t + \psi_i^0\right)\beta_{\mathrm{yaw}} \\ &= A\cos\left(\omega_r t + \psi_i^0\right)\sin(\omega_e t) \\ &\quad + A\sin\left(\omega_r t + \psi_i^0\right)\sin(\omega_e t \pm \pi/2) \\ &= A\sin\left[(\omega_r \pm \omega_e)t + \psi_i^0\right] \end{aligned} \tag{6}$$

where ψ_i^0 is the phase shift originating from the azimuthal position of blade $i = 1, 2, 3$ at time $t = 0$. Generally, the CCW helix results in higher farm-level energy gains [9], [10], while the CW helix is favored for lower damage to the pitch bearing [20], which can be explained by the lower effective actuation frequency of $1P - f_e$.

TABLE I
DEMODULATED LOADS IN EACH REFERENCE FRAME

Load	Coordinate frame		
	Rotating	Fixed	Helix
Wind-induced rotor asymmetry	$1P$	DC	f_e
Helix	$1P \pm f_e$	f_e	DC

A consequence of employing the helix approach is the generation of periodic loading, which impacts the fatigue life of the actuating turbine [20]. This loading, however, is also found on the downstream turbine, as reported by [8]. As such, it negatively impacts the fatigue life of the downstream turbine as well but could potentially be attenuated using a downstream helix load regulator. A different solution to this periodic loading would be to exploit the gain at this frequency to enforce wake mixing further downstream by amplifying the load slightly while preserving its phase. Both these ideas are developed in Section III.

III. NOVEL DOWNSTREAM CONTROLLERS

This section presents the main contributions of this work, the derivation of a downstream helix load regulator, and a phase synchronization control scheme.

A. Downstream Helix Load Regulator

Now, the derivation of the novel downstream helix load regulator is performed. The principle of modulation–demodulation is applied to transform the rotating coordinate frame of the pitch control system to the helix coordinate frame, which demodulates the to-be-attenuated $1P + f_e$ load[1] to the dc gain. This diverges from the conventional MBC transformation, which maps to the fixed coordinate frame (1P frequency to dc gain). In the helix coordinate frame, the helix load can be regulated using two simple integrator control loops. An overview of the loads and their demodulated frequencies in different coordinate frames is given in Table I.

Let the MBC transformation (1) now include the excitation frequency ω_{e} to map to the helix coordinate frame, we have

$$\begin{bmatrix} M_{\mathrm{col,e}} \\ M_{\mathrm{tilt,e}} \\ M_{\mathrm{yaw,e}} \end{bmatrix} = T_{\mathrm{cm}}(\omega_{\mathrm{t}} t) \begin{bmatrix} M_1 \\ M_2 \\ M_3 \end{bmatrix} \tag{7}$$

where

$$T_{\mathrm{cm}}(\omega_{\mathrm{t}} t) = \frac{2}{3}\begin{bmatrix} 1/2 & 1/2 & 1/2 \\ \cos(\psi_1 + \omega_{\mathrm{e}} t) & \cos(\psi_2 + \omega_{\mathrm{e}} t) & \cos(\psi_3 + \omega_{\mathrm{e}} t) \\ \sin(\psi_1 + \omega_{\mathrm{e}} t) & \sin(\psi_2 + \omega_{\mathrm{e}} t) & \sin(\psi_3 + \omega_{\mathrm{e}} t) \end{bmatrix}$$

where $M_{\mathrm{col,e}}$, $M_{\mathrm{tilt,e}}$, and $M_{\mathrm{yaw,e}}$ are the orthogonal moment axes in the helix coordinate frame and $\omega_{\mathrm{t}} = \omega_{\mathrm{r}} + \omega_{\mathrm{e}}$.

[1]In the remainder of this article, the CCW helix load of $1P + f_e$ is assumed, but note that this value can be substituted for CW helix or any desired frequency that acts on the turbine rotor.

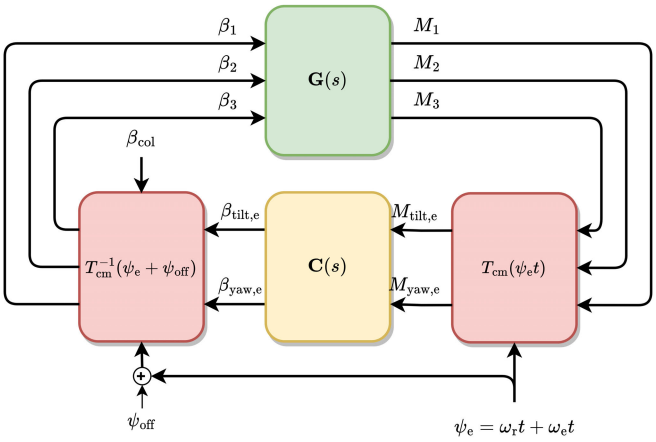

Fig. 1. Proposed control scheme in closed loop.

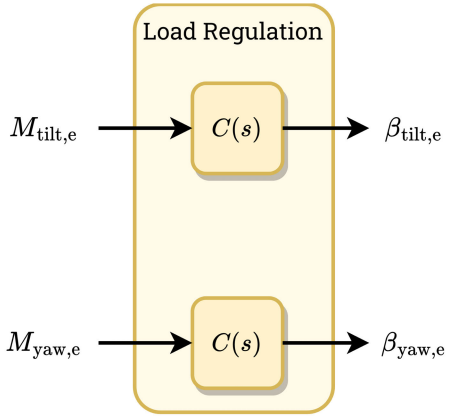

Fig. 2. Controller architecture 1: load regulation scheme.

For ease of implementation, it is useful to decompose $T_{\text{cm}}(\omega_{\text{t}} t)$; thus, the angle sum identity is used

$$\begin{bmatrix} \cos(\omega_{\text{r}} t + \omega_{\text{e}} t) \\ \sin(\omega_{\text{r}} t + \omega_{\text{e}} t) \end{bmatrix} = \begin{bmatrix} \cos(\omega_{\text{e}} t) & -\sin(\omega_{\text{e}} t) \\ \sin(\omega_{\text{e}} t) & \cos(\omega_{\text{e}} t) \end{bmatrix} \begin{bmatrix} \cos(\omega_{\text{r}} t) \\ \sin(\omega_{\text{r}} t) \end{bmatrix}. \quad (8)$$

This allows the decomposition of (7) into

$$\begin{bmatrix} M_{\text{col,e}} \\ M_{\text{tilt,e}} \\ M_{\text{yaw,e}} \end{bmatrix} = \underbrace{\begin{bmatrix} 1 & 0 & 0 \\ 0 & \cos(\omega_{\text{e}} t) & -\sin(\omega_{\text{e}} t) \\ 0 & \sin(\omega_{\text{e}} t) & \cos(\omega_{\text{e}} t) \end{bmatrix}}_{R(\omega_{\text{e}} t)} \times \underbrace{\frac{2}{3} \begin{bmatrix} 1/2 & 1/2 & 1/2 \\ \cos(\psi_1) & \cos(\psi_2) & \cos(\psi_3) \\ \sin(\psi_1) & \sin(\psi_2) & \sin(\psi_3) \end{bmatrix}}_{T_{\text{cm}}(\psi(t))} \begin{bmatrix} M_1 \\ M_2 \\ M_3 \end{bmatrix} \quad (9)$$

with $R(\omega_{\text{e}} t)$ as a rotation matrix. Following a similar methodology, the reverse transformation is found as follows:

$$\begin{bmatrix} \beta_1 \\ \beta_2 \\ \beta_3 \end{bmatrix} = \underbrace{\begin{bmatrix} 1 & \cos(\psi_1) & \sin(\psi_1) \\ 1 & \cos(\psi_2) & \sin(\psi_2) \\ 1 & \cos(\psi_3) & \sin(\psi_3) \end{bmatrix}}_{T_{\text{cm}}^{-1}(\psi(t))} \times \underbrace{\begin{bmatrix} 1 & 0 & 0 \\ 0 & \cos(\omega_{\text{e}} t) & \sin(\omega_{\text{e}} t) \\ 0 & -\sin(\omega_{\text{e}} t) & \cos(\omega_{\text{e}} t) \end{bmatrix}}_{R^{-1}(\omega_{\text{e}} t)} \begin{bmatrix} \beta_{\text{col,e}} \\ \beta_{\text{tilt,e}} \\ \beta_{\text{yaw,e}} \end{bmatrix}. \quad (10)$$

The above-mentioned derivation shows that mapping to the helix coordinate frame is, in fact, a time-varying rotation applied to the system in the fixed coordinate frame. A schematic overview of the proposed control scheme in the helix coordinate frame is shown in Fig. 1. Here, $M_{\text{tilt,e}}$ and $M_{\text{yaw,e}}$ are regulated using two SISO loops, which are schematically depicted in Fig. 2. Note that low-level controllers convert the commanded blade pitch setpoints to hydraulic actuation. Since their dynamics are fast compared with the upper level controller, they are unmodeled. Section IV will elaborate on the synthesis of these SISO controllers.

Section III-B will show that, instead of attenuating the load caused by the actuating upstream turbine as derived earlier, the downstream turbine could also amplify this load, potentially leveraging the periodic content wake to extend the wake mixing further downstream.

B. Downstream Helix Phase Synchronization

The control architecture of the downstream helix load regulator may be extended to obtain a reference tracking controller, which can achieve phase synchronization with the load generated by the incoming wake. This is achieved by setting a reference to the $M_{\text{tilt,e}}$ and $M_{\text{yaw,e}}$ signals. Since the objective is phase synchronization, the phase should be preserved. Therefore, it is first extracted from the measured signals as follows:

$$\phi_{\text{e}} = \text{atan2}\big(M_{\text{tilt,e}}, M_{\text{yaw,e}}\big). \quad (11)$$

Subsequently, an amplitude reference $\mathbf{M}_{\mathbf{e}}^{\text{ref}}$ is defined, which, for amplification, and thus, the propagation of the wake mixing strategy, should be set larger than the amplitude of the measured signals

$$\mathbf{M}_{\mathbf{e}}^{\text{ref}} > \mathbf{M}_{\text{e}} = \left\| \begin{bmatrix} M_{\text{tilt,e}} \\ M_{\text{yaw,e}} \end{bmatrix} \right\|_2. \quad (12)$$

The error is then obtained as follows:

$$\mathbf{M}_{\mathbf{e}}^{\text{err}} = \mathbf{M}_{\text{e}} - \mathbf{M}_{\mathbf{e}}^{\text{ref}}. \quad (13)$$

Finally, the error signals are constructed as

$$\begin{bmatrix} M_{\text{tilt,e}}^{\text{err}} \\ M_{\text{yaw,e}}^{\text{err}} \end{bmatrix} = \mathbf{M}_{\mathbf{e}}^{\text{err}} \begin{bmatrix} \sin(\phi_e) \\ \cos(\phi_e) \end{bmatrix} \quad (14)$$

which preserves the phase of the periodic load. The control architecture of the phase synchronization method is schematically displayed in Fig. 3.

IV. Controller Synthesis

After deriving the novel coordinate transformation in Section III, this section aims to synthesize suitable proportional–integral–derivative (PID) controllers for the system in this framework through loop shaping. First, a linear model of the system (described in Section V) in helix coordinates is identified by means of black box system identification.

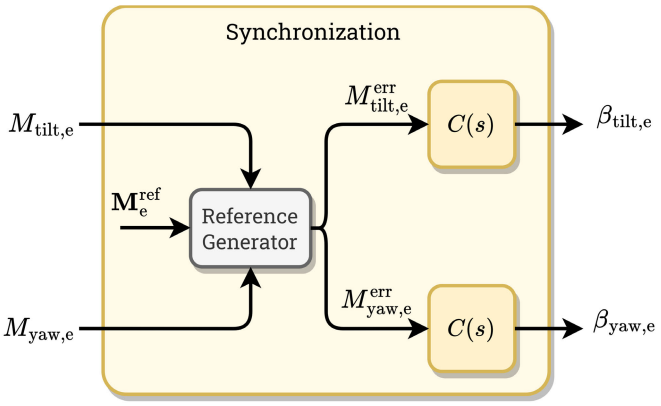

Fig. 3. Controller architecture 2: helix synchronization scheme.

Then, using the identified model, PID controllers are tuned by using classical loop shaping techniques.

To identify a model, the optimized predictor-based subspace identification (PBSID$_{\text{opt}}$) [21] method is used—an algorithm based on the well-known stochastic subspace identification method. This approach uses input–output data to estimate a linear model, which is obtained by persistently exciting the system with an input signal containing a broad spectrum of frequencies. As an excitation signal, pseudorandom binary noise is chosen, which is bandpass-filtered between 1e-3 and 1e2 rad/s to accommodate the actuator bandwidth. A high-fidelity LES, using the simulation settings specified in Section V, is run to obtain the input–output data. Since a linear identification method is used, the obtained model is linear-time invariant and, therefore, only valid for a specific operating range.

The singular values yielded by the PBSID$_{\text{opt}}$ method assist in determining an optimal identification order, where an order of ten was found to correspond best to the spectral average of the input–output data, as can be observed in Fig. 4. Note the difference in steady-state magnitude between the diagonal and off-diagonal transfers, denoting the degree of coupling the system has. A low coupling is desired, which simplifies controller synthesis as an SISO control loop can be used on each diagonal transfer. In this work, an azimuth offset of $\psi_{\text{off}} = 8$ degrees is used to facilitate further decoupling [18]. However, the identified model is based on standalone OpenFAST, while further decoupling may be required if coupled to LES [22]. Further optimization of the optimal azimuth offset, however, is out of the current scope.

To control the loads at the ω_{t} frequency, the following diagonal SISO control structure is designed, as shown in Figs. 2 and 3

$$\begin{bmatrix} \beta_{\text{tilt,e}}(s) \\ \beta_{\text{yaw,e}}(s) \end{bmatrix} = \underbrace{\begin{bmatrix} C(s) & 0 \\ 0 & C(s) \end{bmatrix}}_{\mathbf{C}(s)} \begin{bmatrix} M_{\text{tilt,e}}(s) \\ M_{\text{yaw,e}}(s) \end{bmatrix} \tag{15}$$

where $\mathbf{C}(s)$ is shown in Fig. 2.

The tuning of PID controllers is done by frequency-domain loop shaping the transfer of the identified model and controller to achieve a certain crossover frequency ω_c

$$L(s) = G(s)C(s) \tag{16}$$

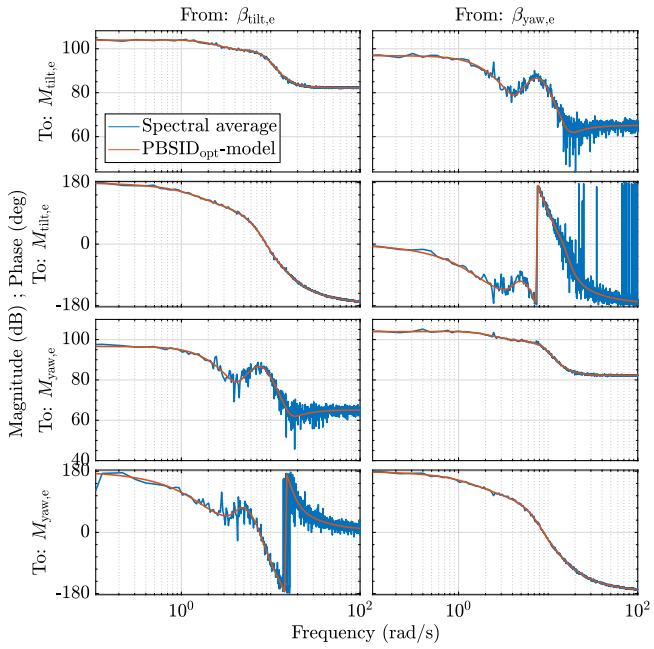

Fig. 4. Comparison of the PBSID$_{\text{opt}}$-identified model against the spectral averaged input–output data.

TABLE II
CONTROLLER PARAMETERS

Controller	K_{P} [rad/Nm]	K_{I} [rad^2/(Nms)]	ω_{lpf} [rad/s]
C_{I_1}	-	7.9e-10	-
$C_{\text{PI-LPF}_1}$	1.1e-8	1.34e-11	1
$C_{\text{PI-LPF}_2}$	1.1e-8	1.32e-11	0.0718
C_{I_2}	-	1.34e-11	-

where $L(s)$ is the loop transfer and $G(s)$ is the plant of the system in the helix coordinate frame. A crossover frequency of $\omega_c = 0.115$ rad/s provided a good tradeoff between transient response and sensitivity to noise for the initial controller design. Further adjustments in other controller concepts either increased or decreased this value. Two different types of controllers are implemented in (15); an integrator controller and a proportional–integral with low-pass filter (PI-LPF) controller

$$C_{\text{I}}(s) = \frac{K_{\text{I}}}{s} \tag{17}$$

$$C_{\text{PI-LPF}}(s) = \frac{K_{\text{P}}\omega_{\text{lpf}}(s + K_{\text{I}}/K_{\text{P}})}{s\left(s + \omega_{\text{lpf}}\right)} \tag{18}$$

where the chosen tuning parameters are provided in Table II and the resulting Bode plots of the controllers are given in Fig. 5.

Since only a bias is corrected, an integral controller (17) may already be sufficient as it corrects the steady-state error. Two different gains are examined here to compare different levels of aggressiveness. However, if the error signal contains too rapid changes, possibly due to nonideal conditions, such as turbulence or gusts, a PI controller may respond better to the immediate error. Nevertheless, this may increase actuator costs due to the high-frequency content included in the control action. Thus, a tradeoff between smooth control performance and actuator activity may be accommodated by the PI-LPF

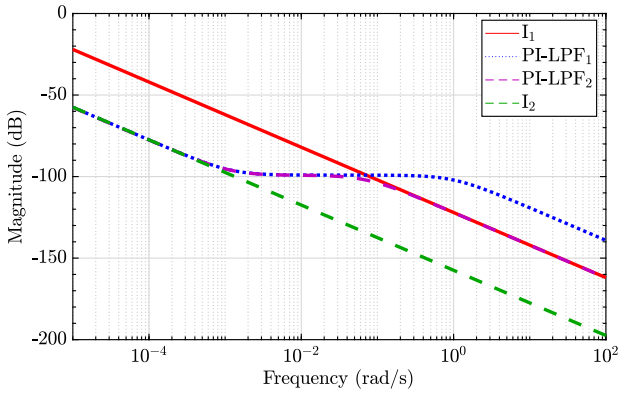

Fig. 5. Comparison of the Bode plots of the different controller types.

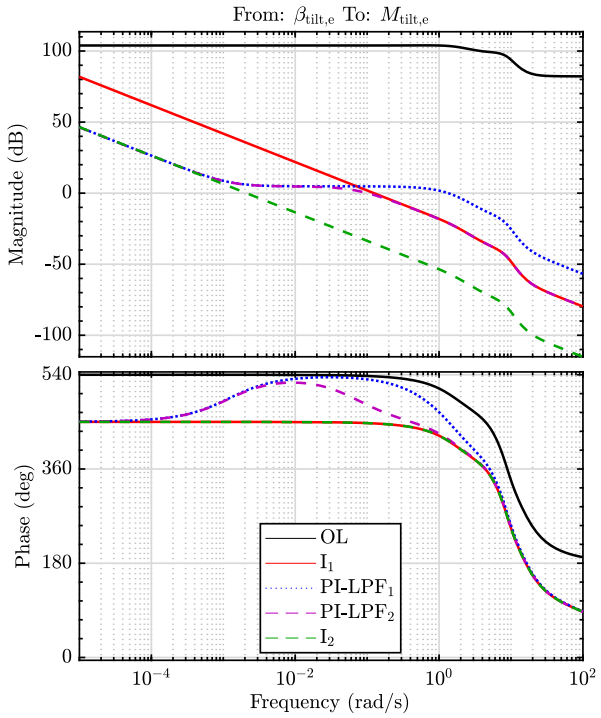

Fig. 6. Comparison of the different loop transfers, including different controller types. OL denotes the open-loop system.

controller (18), which is evaluated here for different combinations between the K_{I}, K_{P}, and ω_{lpf} parameters. The resulting helix frame loop transfers in the discrete-time domain with zero-order hold discretization method where sampling time $dt = 0.005$ s is used, is shown in Fig. 6.

Note that these controllers are not fully optimized and are selected to study the effect of different controller concepts. More advanced controller synthesis may yield better performance and is the subject of future work. Additionally, no form of antiwindup is present in the PID controllers. However, the integrator term is saturated to prevent it from growing too large.

V. Simulation Setup

The effectiveness of the controllers is studied in a high-fidelity simulation environment, where the aero–hydro–servo–elastic wind turbine tool OpenFAST (fatigue, aerodynamics, structures, and turbulence) [23] is coupled to the high-fidelity fluids solver adaptive mesh refinement (AMR)-wind to perform coupled LES. This section introduces these codes and presents the simulation settings used in this study.

TABLE III
Specifications of the IEA 15-MW Reference Turbine

Characteristic	Value
Hub height	150 m
Rotor diameter	240 m
Rated power	15 MW
Rated wind speed	10.59 m/s
Cut-in wind speed	3 m/s
Cut-out wind speed	25 m/s
Min. rotor speed	5 rpm
Max. rotor speed	7.56 rpm

A. OpenFAST Simulation Setup

OpenFAST is a multifidelity wind turbine simulation tool coupling several standalone modules relating to different aspects of wind turbine simulation, including the structural dynamics, control system, hydrodynamic, and aerodynamics loads. The aerodynamic loads can be computed through computationally efficient engineering models, such as the blade element momentum (BEM) theory model, or higher fidelity models, such as free-vortex methods, or flow solvers like AMR-Wind.

The current work evaluates the proposed controllers on the International Energy Agency's (IEA), Paris, France, 15-MW fixed-bottom reference wind turbine [24]. This turbine is controlled using the reference open-source controller (ROSCO) [25], which is modified to include the proposed control scheme.[2] Some specifications of this turbine are given in Table III. The OpenFAST model of this turbine is used in this work, whose specifications are consistent with those listed in Table III.

The OpenFAST simulation is coupled to the LES through the actuator line method (ALM) [26], where the turbine blades are represented as lines composed of discrete segments along their span. Each segment is associated with an "actuator," which is a mathematical representation of the forces applied by that part of the blade on the fluid. These forces influence the local flow conditions, such as velocity, pressure, and turbulence.

Even though the ALM allows more computationally efficient LES, the simulation requires significant resources and runs at a time step of 0.05 s, while the OpenFAST simulation runs at a smaller time step of 0.005 s, where interpolation is performed to facilitate the data exchange. Note that the interpolation in coupled LES introduces phase lags to the controller, which increases the optimal azimuth offset. An additional phase correction may be necessary to fully decouple the pitch control system, ensuring optimal controller performance [22].

[2]https://github.com/mvanv/ROSCO/tree/WakeMixingLoadIPC

B. AMR-Wind Simulation Setup

AMR-wind is a parallel adaptive-mesh solver for incompressible flow built on the AMReX library and specifically targeted for wind energy [27]. The software enables LES of atmospheric boundary layer (ABL) flows, wind farm turbine-wake interactions, and blade-resolved simulations of multiple turbines within a wind farm and is, therefore, very suited for evaluating controllers that rely on the interaction between wind turbines, such as the controller proposed in this article. For details regarding the governing equations and wall models of AMR-wind, the reader is referred to [28].

In this work, and similar to previous work [10], a convective boundary layer (CNBL) precursor, including Coriolis force effects, is investigated, where the ABL interacts with a stable stratified free atmosphere characterized by a lapse rate of 1 K/km. As recommended in [29], a capping inversion is employed to control the growth and height, where the boundary layer height (h) is set at 1000 m, with a surface roughness (z_0) of 0.0002 m based on offshore measurements in The Netherlands [30]. The LES used for system identification does not leverage the CNBL but instead uses laminar flow with a wind speed similar to the mean wind speed acting on the downstream turbine in the CNBL simulation, which ensures a cleaner identified model.

For the precursor simulation, the domain size is $x = 5360$,m, $y = 3200$ m, and $z = 1600$ m, accommodating three turbines. The isotropic grid size is 10 m, meeting CNBL requirements [31]. Using periodic boundary conditions, the flow evolves for 16 h, establishing a quasi-stationary turbulent ABL state [32].

Subsequently, during the next 45 min, yz planes are sampled at the inflow ($x = 0$ m) as inflow boundary conditions for turbine simulations. These simulations are enabled through the ALM coupling with OpenFAST.

In the domain, the three turbines are placed at ($x = 1200$ m, $y = 1600$ m), ($x = 2400$ m, $y = 1600$ m), and ($x = 3600$ m, $y = 1600$ m), for turbine 1 (T1), T2, and T3, respectively, accommodating a 5-D spacing from the inflow and a 5-D spacing between the turbines, while leaving sufficient space for the wake behind the third turbine to develop. A spacing of 5-D corresponds to the distance between the turbines of the Hollandse Kust Noord Wind Farm, The Netherlands [33], but the spacing of a wind farm can be as small as 3.3–4.3-D for the Lillgrund Wind Farm, Sweden, resulting in much higher wake losses [34]. A large spacing is more beneficial for wake recovery but requires more surface area, decreasing energy density. A spacing between 3–7-D is usually a tradeoff in farm layout design between costs due to wake losses and costs for larger spacing such as cabling and land use. Wake mixing techniques, such as the helix approach, could facilitate closer spacings in the future due to faster wake recovery, thereby increasing energy density.

A mesh refinement to 5 m is set surrounding the three turbines in a static box with size $x_m = 5040$ m, $y_m = 960$ m, and $z_m = 600$ m starting 4.5-D upstream of the first turbine to enable higher resolution flow surrounding the wind turbines. A snapshot for illustration of one LES is given in Fig. 7. Note the highly resolved flow showing wake characteristics, such as meandering, due to the helix actuation strategy.

Each LES is run on the supercomputer DelftBlue [35] and is run parallelized on 528 processors with 4GB of memory each. The total real-time duration of each simulation is approximately 48 h.

TABLE IV
OVERVIEW OF THE CONTROLLERS USED IN EACH TEST CASE

Case	T1	T2	T3	Ref. [kNm]
BL Helix	CCW Helix	Greedy	Greedy	n.a.
TC1	CCW Helix	I_1-Rej.	Greedy	n.a.
TC2	CCW Helix	PI-LPF$_1$-Rej.	Greedy	n.a.
TC3	CCW Helix	PI-LPF$_2$-Rej.	Greedy	n.a.
TC4	CCW Helix	I_2-Rej.	Greedy	n.a.
TC5	CCW Helix	I_1-Track.	Greedy	1e4
TC6	CCW Helix	PI-LPF$_1$-Track.	Greedy	1e4
TC7	CCW Helix	PI-LPF$_2$-Track.	Greedy	1e4
TC8	CCW Helix	I_2-Track.	Greedy	1e4
TC9	CCW Helix	PI-LPF$_1^+$-Track.	Greedy	1.2e4

C. Test Cases

To study the effect of the proposed control scheme on the loads and power production, ten coupled LES are performed (Table IV). A baseline helix case is performed, where a CCW helix with 4° amplitude and $S_t = 0.25$ is initiated on the first turbine, while the second and third operate with their baseline "greedy" control strategy. The greedy wind turbine control strategy aims to maximize the immediate power output of a single wind turbine by dynamically adjusting the blade pitch angle and generator torque in real time. Below the rated wind speed, it increases rotor speed by keeping the blade pitch constant and adjusting the torque, while above the rated wind speed, it maintains optimal rotor speed by increasing the blade pitch to reduce aerodynamic load. This straightforward approach is advantageous for its simplicity and standard in most wind farms. The helix settings were to match the original settings from [9] but may be further optimized as desired. The first four test cases evaluate the rejection control strategy to drive the helix load to zero using the controllers described in Table II. The next four test cases evaluate the tracking control strategy using the same controller types, where a reference $\mathbf{M_e^{ref}} = 1e4$ kNm is set, which is double the value it attains during the baseline case. Note that this reference value is not optimized here to maximize a power/loads tradeoff due to the computational cost of LES. However, a single test case with an increased amplitude reference $\mathbf{M_e^{ref}} = 1.2e4$ kNm is run, which is analyzed in terms of power and loads.

VI. RESULTS: REJECTION SCHEME

This section presents the findings of the investigation into the rejection scheme's performance by evaluation of TC1–TC4, which employ different PID controllers. The analysis encompasses evaluating the controller's rejection performance, assessment of the required pitch actuator actions, and analysis of the damage-equivalent loads (DELs) per industry practice.

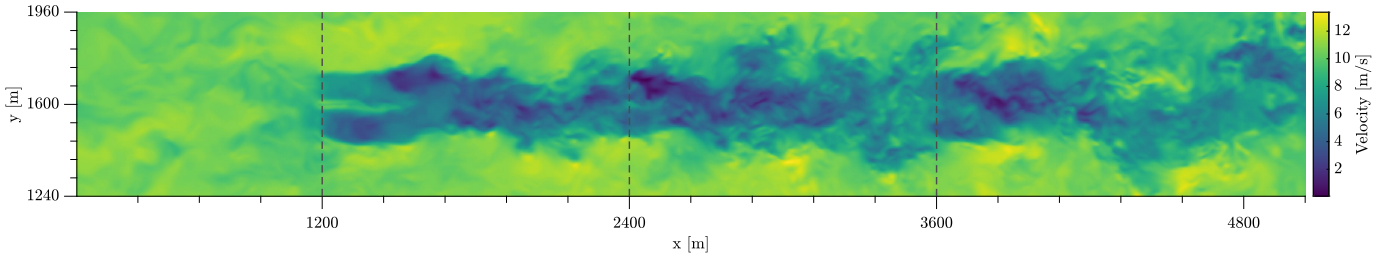

Fig. 7. Vertical slice of the static box refinement at $t = 59\,800$ s showing velocity in the x-direction for test case 6. The turbines are placed at the dashed lines.

A. Analysis of Controller Performance

Here, the controller performance is evaluated by investigating the system response in both the frequency and time domains.

Fig. 8 displays the rotor loads in different reference frames, with M_1 in the rotating frame, M_{tilt} in the fixed frame, and $M_{\text{tilt,e}}$ in the helix frame.[3] The left column shows the frequency-domain representation of these signals in the form of a power spectrum, while the right column presents low-pass filtered time series data.

The objective of the rejection controller is to drive the helix load toward zero. In the frequency domain plots, this can be observed by inspecting the helix load in the different reference frames. Note that the helix and wind-induced rotor-asymmetric load appear at different locations in the different frames (see Table I). A clear difference is notable between the aggressiveness of the controllers, where the I_2 controller shows much less attenuation compared to, e.g., the I_1 controller. However, all controllers are able to reduce the helix load significantly compared with the baseline case.

In the time domain, this difference in aggressiveness becomes clear as well, where it can be seen that most controllers successfully drive the bias in $M_{\text{tilt,e}}$, which is present in the baseline case, toward zero. In contrast, the I_2 controller only appears to do so to a slight extent.

Interestingly, the wind-induced rotor asymmetric load, which is present in the baseline case, appears to be reduced by the proposed controllers as well, benefiting the fatigue life even more. Note that the less aggressive I_2 controller does not attenuate this load. This observation is also clearly visible in the rotating frame, where this load appears at the $1P$ frequency.

To further understand the reason why some controllers correct the wind-induced rotor asymmetric load as well, the sensitivity function of the $\beta_{\text{tilt,e}}$ to $M_{\text{tilt,e}}$ transfer in the helix frame is studied in Fig. 9. The sensitivity function is given by

$$\frac{1}{1 + G(s)C(s)}. \tag{19}$$

This function provides insights into the controller's effectiveness across various frequencies. The objective is to maintain a consistent gain of 0 dB across all frequencies while attenuating the dc gain, where the helix load acts in the helix coordinate frame. In Fig. 9, it becomes evident that the controllers adeptly mitigate lower frequencies, aligning with the desired behavior. However, a closer observation reveals that the I_1-, PI-LPF$_1$, and PI-LPF$_2$-controllers introduce some attenuation to f_e, which explains the behavior of these controllers in reducing the wind-induced rotor asymmetric load.

It should be noted that the control settings and tuning significantly impact the controller's performance. For example, if a large Strouhal number is selected, the wind-induced rotor asymmetric load is at a significantly higher frequency in the helix frame, which might not be attenuated by any of the current controllers. Or, if different gains are chosen, the region of attenuation may become smaller or larger. Therefore, if the objective is to reduce both the wind-induced rotor asymmetric load and helix load, a careful methodology should be followed to ensure both are mitigated as desired. Possibly more advanced H_2- or H_∞-control could provide more effective solutions (see [36]).

In summary, the load rejection scheme effectively mitigates the helix load present in the baseline case in most control setups while also attenuating the wind-induced rotor asymmetric load in the most aggressive controllers, as demonstrated by both time- and frequency-domain analyses. These results show promising indications for enhancing the fatigue life of the downstream turbine, which is further analyzed in Section VI-B by quantifying the DELs and pitch bearing damage (PBD).

B. Impact on Power Production, DELs, and PBD

This section quantifies the improvement of the fatigue life of T2 and T3 due to the proposed controller by computation of the DELs and comparison against the baseline helix case. This metric allows a comparison of the degree of loading a turbine encounters during the simulation and complies with the industry convention according to the IEC-61400 standard [37]. It further relies on the rainflow-counting algorithm and is computed through the following formula:

$$\text{DEL} = \left(\frac{\sum_{i=1}^{N} (A_i)^m n_i}{n_{\text{eq}}} \right)^{\frac{1}{m}} \tag{20}$$

where N is the total count of cycles, m is the inverse Wöhler slope, conventionally taken as 5 for steel tower components and 10 for composite blade structures. Moreover, n_i indicates the number of cycles represented by a range of A_i, and n_{eq} denotes the equivalent cycle, set to 1 here.

[3] As the conclusions drawn from the results of the orthogonal channels (yaw, yaw$_e$) and blade 2 and 3 are similar, they are omitted in the remainder of this article for conciseness but available upon request.

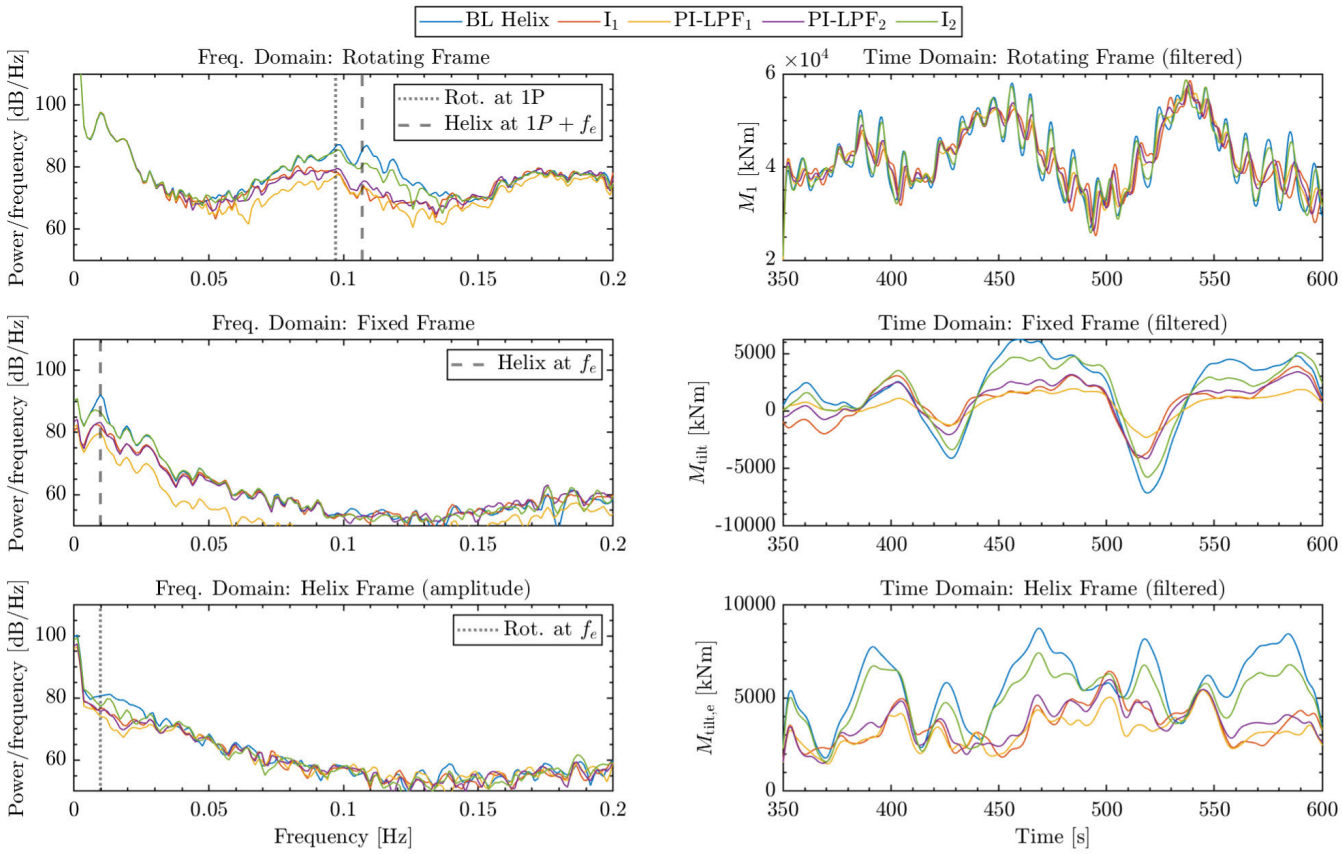

Fig. 8. Comparison of the blade loads of T2 in different reference frames in the frequency and time domains. The left column shows the frequency-domain representation of these signals, highlighting the reduction in helix load and wind-induced rotor asymmetric load in the helix frame due to the rejection controllers. The right column presents low-pass filtered time series data, indicating the successful driving of the bias in $M_{\text{tilt,e}}$ toward zero for most controllers.

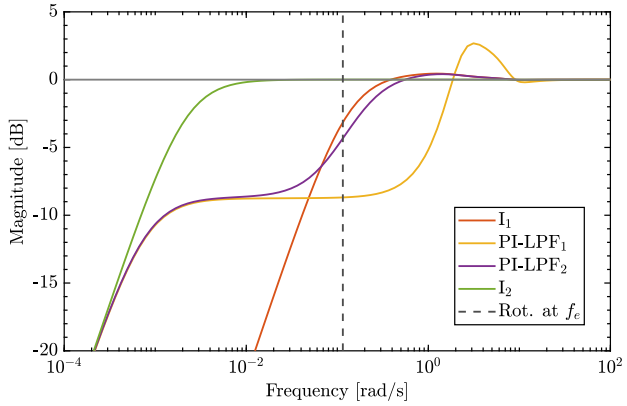

Fig. 9. Sensitivity function of the rejection controller.

The first 350 s of the dataset are discarded to account for the propagation of the wake from the upstream to the downstream turbine and other transient effects in the simulation. A total of 2150 s of simulation time is used in the DEL calculations.

Fig. 10(b) and (c) shows the results of the DEL calculations, where the DEL of the controllers is displayed relative to the baseline helix case. It is evident from the bar graph that there are significant disparities in the reduction in loads between the different controllers. All controllers show a substantial decrease in DEL. However, this reduction does not come without costs, as the I_1-controller causes a notable reduction in power, and others also see a slight power decrease [Fig. 10(a) and Table V]. The I_2 and PI-LPF$_1$ appear to strike the best balance between load reduction and power production preservation.

TABLE V
OVERVIEW OF THE POWER GAINS UNDER THE DIFFERENT CONTROLLERS

Controller	T2 [MW]	T3 [MW]	T2+T3 [MW]
I_1-rejection	6.93 (-1.83%)	6.77 (-1.27%)	13.71 (-1.56%)
PI-LPF$_1$-rejection	6.99 (-1.06%)	6.88 (+0.23%)	13.86 (-0.42%)
PI-LPF$_2$-rejection	6.97 (-1.30%)	6.84 (-0.28%)	13.81 (-0.80%)
I_2-rejection	7.03 (-0.54%)	6.85 (-0.20%)	13.87 (-0.37%)

Interestingly, also the third turbine experiences substantial load reductions for most controllers. Even for the case where the third turbine experiences a small power gain, with the PI-LPF$_1$ controller, there is a load reduction visible on the third turbine, while usually, an increase in power is associated with a DEL increase.

Another metric used to study fatigue is PBD. This is damage that builds up in the pitch actuators over time and can be understood as the cost of the control action that is required to achieve the control objective. The formula is given by [20]

$$\text{PBD}(\gamma) = \sum_{k=1}^{N} \delta\theta(k)\left(\max\left(\cos(\gamma)M_{\text{flap}}(k) + \sin(\gamma)M_{\text{edge}}(k), 0\right)\right)^m \tag{21}$$

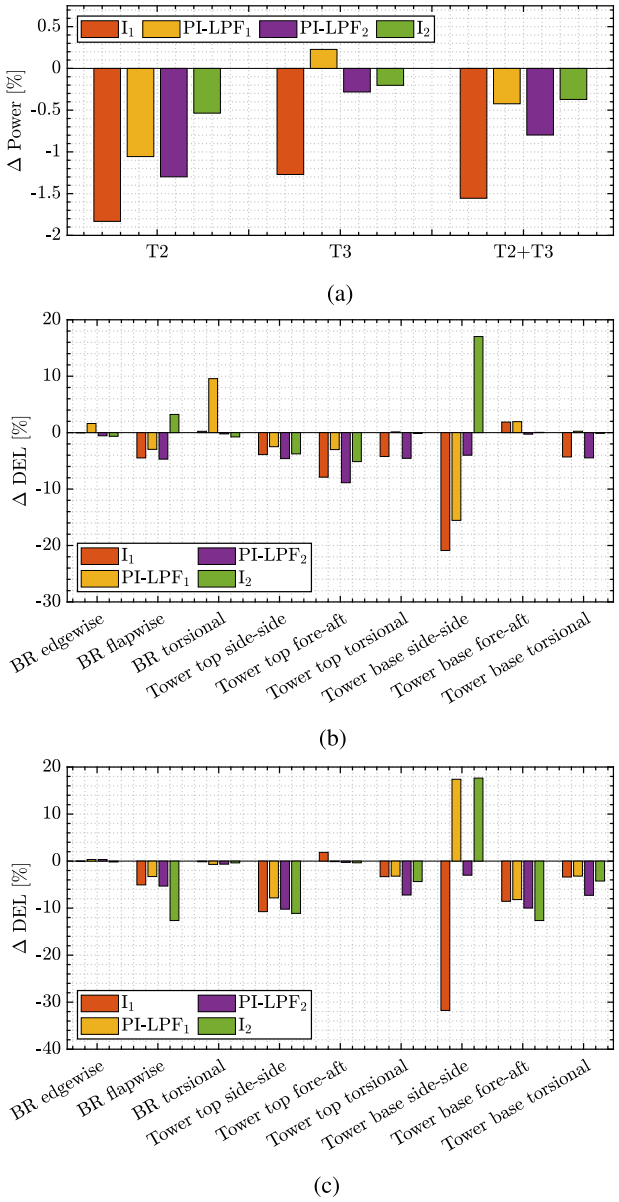

Fig. 10. Performance plots of the rejection controllers. (a) Bar chart of the power difference relative to the baseline helix case for T2, T3, and combined. (b) Bar chart of the DELs of the rejection controllers relative to the baseline helix case for T2. "BR" denotes blade root. (c) Bar chart of the DELs of the rejection controllers relative to the baseline Helix case for T3. "BR" denotes blade root.

where γ is the radial position of the bearing, $\delta\theta$ is the pitch difference, M_{flap} is the flapwise blade root moment, M_{edge} is the edgewise blade root moment, and m is the inverse Wöhler slope. Here, only the radial position with the largest damage is examined.

The computed PBDs are displayed in Table VI, which are compared against the PBD of T1. It can be observed that the PBD of T1 is very high compared with the PBD of T2, employing the rejection controllers while actuating with similar pitch amplitude and frequency. The strong difference in wind speed increasing the blade root moment on T1 plays a role here, but another important cause is the reduction in the blade root moment on T2 as a result of the I_1-rejection controller. Observe in (21) that it is a function of the blade root moments. Even though significant pitch action is required,

TABLE VI
OVERVIEW OF THE PBDS UNDER THE DIFFERENT CONTROLLERS

Turbine	Controller	PBD ($\times$1e^{17}) [kNm^3 deg]
T1	BL Helix	20.17
T2	I_1-rejection	0.78
	PI-LPF$_1$-rejection	1.76
	PI-LPF$_2$-rejection	0.63
	I_2-rejection	0.52

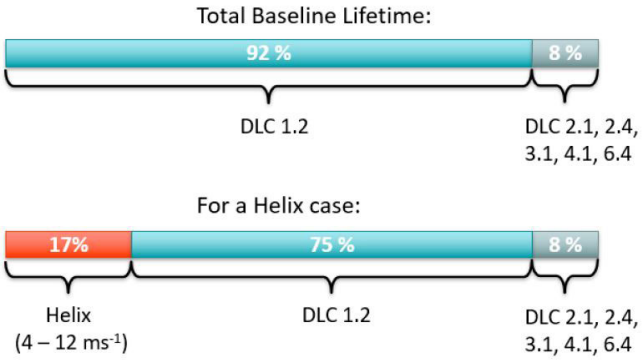

Fig. 11. Comparison between the division of DLCs of the baseline greedy versus baseline helix case in [38].

a reduction of blade root moment prevents a substantial increase in PBD on T2, significantly alleviating PBD concerns regarding the implementation of this method.

C. Note on Lifetime Fatigue

While the above-mentioned analyses allow comparison between the different control approaches, they do not provide a complete picture of the impact on turbine fatigue life. To properly assess this, a comprehensive loads study is required, evaluating all load cases as specified in IEC-61400-1. Only the manufacturer possesses the necessary detailed knowledge, including design specifics, material properties, and operational data, to accurately evaluate the impact on fatigue life.

Moreover, since these controllers are active only in specific scenarios (i.e., in a periodic wake), they can only be evaluated accurately using high-fidelity codes, such as LES. These simulations are costly compared with conventional BEM codes used for load calculations. Hence, this study refrains from quantitatively assessing the impact on turbine fatigue lifetime.

A qualitative assessment for the baseline helix case shows that, assuming 17% activation time (based on a study on the Hollandse Kust Noord Wind Farm [38]), the impact on lifetime fatigue for various load channels is shown in Table VII. This assumes design load case (DLC) 1.2 accounts for 75% of operational time, with other DLCs (2.1, 2.4, 3.1, 4.1, and 6.4) covering the remaining 8% (Fig. 11).

Note the relatively strong increase in pitch-bearing lifetime fatigue. This implies the pitch bearing must be replaced twice as often during the turbine lifetime compared with the baseline. Eventually, pitch bearings should be designed, taking fatigue due to wake mixing control into account, which is currently not the case.

Comparing PBDs between the upstream turbine and proposed downstream controllers (Table VI), the downstream approach shows significantly lower PBD, implying only a

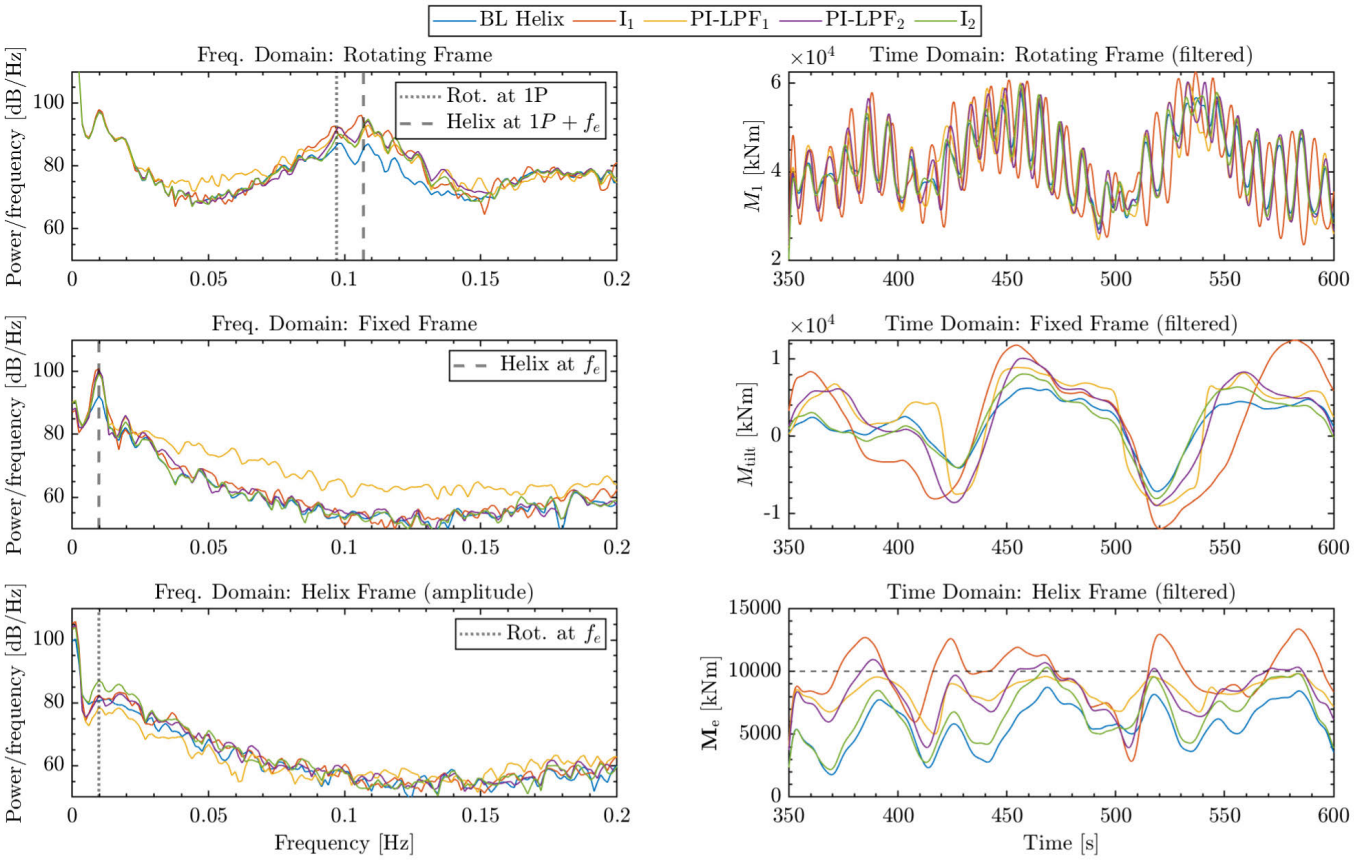

Fig. 12. Comparison of the blade loads of T2 in different reference frames in the frequency and time domains. The left column shows the frequency-domain representation of these signals, illustrating the amplification of the helix frequency due to the tracking controllers. The right column presents low-pass filtered time series data, indicating the phase synchronization capabilities of the controllers. The reference in the lower right plot is indicated by the horizontal dashed line.

TABLE VII
OVERVIEW OF THE IMPACT ON LIFETIME FATIGUE FOR BASELINE HELIX

Channel	Lifetime fatigue increase
Blade root edgewise	+0.6%
Blade root flapwise	+1.3%
Tower top side-side	+0%
Tower top fore-aft	+9.4%
Tower top torsional	+4.7%
Tower base side-side	+0.1%
Tower base fore-aft	+0.8%
Pitch bearing	+92.9%

slight overall increase compared with the upstream-only method.

VII. Results: Tracking Scheme

After discussion of the results of the rejection scheme, this section now presents the results obtained when toggling the other objective—synchronized wake mixing for power enhancement, which is achieved by tracking a reference. Here, TC5–TC9 are evaluated and compared, where the tracking performance of the controller, DELs, and PBD are analyzed. Also, some flow analysis is presented and reviewed.

A. Analysis of Controller Performance

This section examines the controller performance by performing time- and frequency-domain investigations of the system's response and control commands.

Fig. 12 displays the rotor loads in different reference frames, with M_1 in the rotating frame, M_{tilt} in the fixed frame, and $\mathbf{M}_\text{e}$ in the helix frame. Rather than analyzing $M_{\text{tilt,e}}$ and $M_{\text{yaw,e}}$, the control performance is better understood when inspecting the amplitude $\mathbf{M}_\text{e}$ since the phase ϕ_e of $M_{\text{tilt,e}}$ and $M_{\text{yaw,e}}$ might change over time. This influences the resulting reference to $M_{\text{tilt,e}}$ and $M_{\text{yaw,e}}$ and makes drawing conclusions in the time domain more challenging. The left column shows the frequency domain representation of these signals in the form of a power spectrum, while the right column presents low-pass filtered time series data.

The objective of the tracking controller is to correct the bias to the reference $\mathbf{M}_\text{e}^\text{ref}$, essentially amplifying the Helix frequency. This amplification can be observed in the frequency domain, where the characteristic peak has increased in the rotating and fixed coordinate frame. In the time domain, an interesting observation of the phase synchronization capabilities can be made, where it appears in the fixed frame in Fig. 12 that the aggressive I_1 controller is not able to match the phase with the baseline Helix case's phase. This implies it does not fully leverage the already present content and needs to compensate to force a different phase in the response, requiring more pitch action.

The PI-LPF$_1$-controller, while synchronizing the phase, has a rather noisy pitch signal, which can be seen from Fig. 13, which depicts the pitch rate. A noisy pitch signal impacts loads on the structure and damages the pitch bearing. Ultimately, the

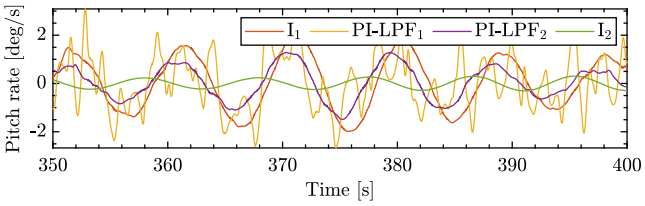

Fig. 13. Comparison of the pitch rate.

PI-LPF$_2$-controller may be considered to show a compromise between the aggressiveness of the I_1-controller and the desired control behavior, as shown by the PI-LPF$_1$-controller. Akin to the PI-LPF$_1$-controller, it can synchronize but does not exercise a high-frequent pitch signal, making it a suitable candidate for the phase-synchronization objective. A target sensitivity Bode plot could be established, demonstrating the suitability of this approach for H_2/H_∞ controller synthesis. Section VII-B quantifies the DELs and PBDs and studies the power production of the test cases.

B. Impact on Power Production, DELs, and PBD

Here, the impact on fatigue life, pitch bearing, and power production is studied. Also, an additional test case, namely, PI-LPF$_1^+$, is examined, in which an increased reference $\mathbf{M_e^{ref}}$ is used. Since the objective is phase synchronization for power enhancement, first, the power production of each control case is investigated in Fig. 14(a). The I_1-tracking controller appears to cause a significant power loss on T2, which may be caused by the inability to fully exploit the periodic wake such that phase synchronization could not always be attained. However, a power increase is observable at T3 as a result of the tracking controller on T2, although it is insufficient to increase the aggregate power capture of both turbines.

Interestingly, a slight power gain can be observed on T2 when employing the other controllers, which suggests that baseline greedy control is potentially not optimal for power extraction when a turbine is in a helix wake, however, more investigation is required to confirm this. Even more striking is the fact that, due to phase synchronization, the wake mixing is continued further downstream and significantly benefits T3 as a significant power gain of 4.39% could be attained for the PI-LPF$_1$-controller, resulting in a 2.3% overall power gain underlining the potential of phase synchronized wake mixing. Similarly, the PI-LPF$_2$ controller shows a power increase, with a considerable power gain of 3.98% on T3, while increasing the total power with 2.01%. The best-performing controller PI-LPF$_1$ was tested with an extended reference referred to as the case PI-LPF$_1^+$, where an even more prominent power increase of 5.96% could be observed on T3 and a collective increase of 2.96%. An overview of the power production for each controller is given in Table VIII.

Next, an analysis is made of the DEL increase for all cases relative to baseline in Fig. 14(b) for T2 and Fig. 14(c) for T3. From Fig. 14(b), it can be concluded that all cases increase the DELs on T2, while the strongest increase is in the I_1-tracking case. For example, the strong increase in DEL on the blade root flapwise moment for the I_1-tracking controller is due to the stronger amplification, while the increases of the PI-LPF$_1$-

TABLE VIII
OVERVIEW OF THE POWER GAINS UNDER THE DIFFERENT CONTROLLERS

Controller	T2 [MW]	T3 [MW]	T2+T3 [MW]
I_1-tracking	6.81 (-3.58%)	6.89 (+0.50%)	13.70 (-1.57%)
PI-LPF$_1$-tracking	7.08 (+0.26%)	7.16 (+4.39%)	14.24 (+2.30%)
PI-LPF$_2$-tracking	7.07 (+0.09%)	7.13 (+3.98%)	14.20 (+2.01%)
I_2-tracking	7.07 (+0.17%)	6.96 (+1.43%)	14.03 (+0.79%)
PI-LPF$_1^+$-tracking	7.07 (+0.05%)	7.27 (+5.96%)	14.34 (+2.96%)

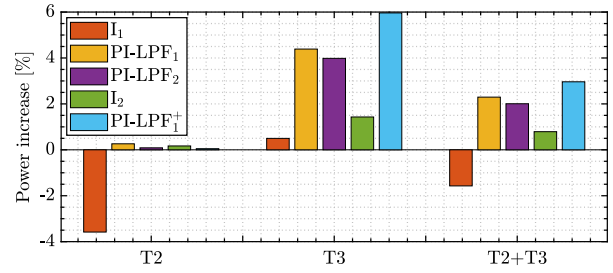

(a)

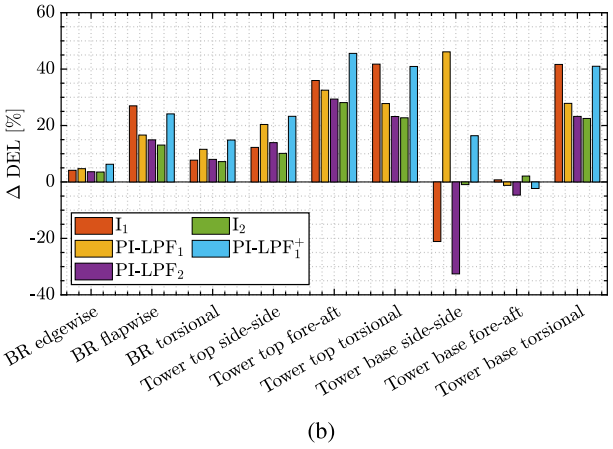

(b)

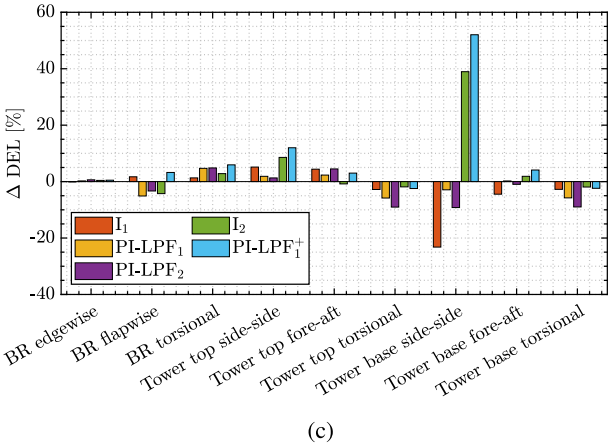

(c)

Fig. 14. Performance plots of the tracking controllers. (a) Bar chart of the power increase relative to the baseline helix case for T2, T3, and combined. (b) Bar chart of the DEL increase relative to the baseline helix case for T2 for the different controllers. (c) Bar chart of the DEL increase relative to the baseline helix case for T3 for the different controllers.

controller are due to the large variations in the pitch actuation, where higher frequent noise propagates to the turbine structure and increases the fatigue damage. In the case of T3, there are no clear trends visible. Generally, when the wind speed is higher due to wake mixing, a slight load increase may be

TABLE IX
OVERVIEW OF THE PBDS UNDER THE DIFFERENT CONTROLLERS

Turbine	Controller	PBD ($\times 1e^{17}$) [kNm^3 deg]
T1	BL Helix	20.17
T2	I_1-tracking	2.23
	PI-LPF$_1$-tracking	1.88
	PI-LPF$_2$-tracking	1.36
	I_2-tracking	1.09
	PI-LPF$_1^+$-tracking	2.28

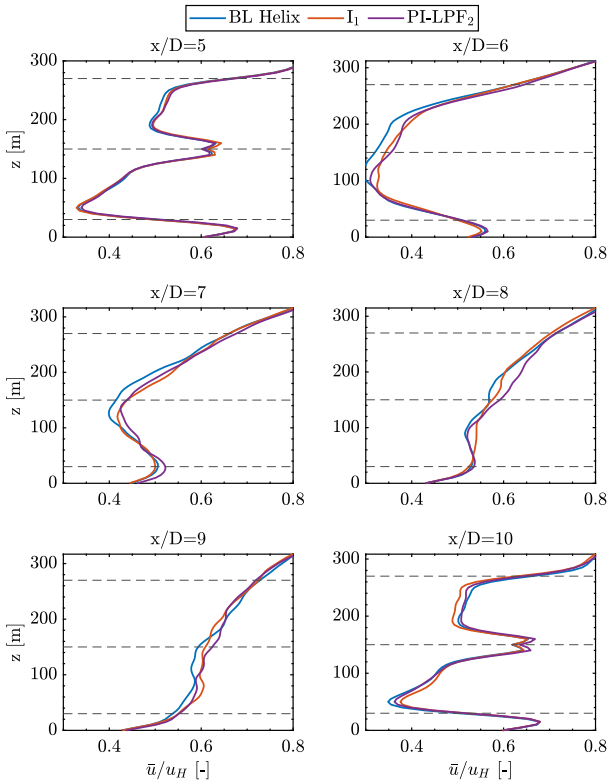

Fig. 15. Vertical profile of the mean streamwise velocity of the wake behind T2 for several rotor distances D behind T2 ($x/D = 5$) for the tracking controllers. The dashed horizontal lines indicate the rotor top, hub, and bottom. T3 is located at $x/D = 10$.

expected on T3, this is, however, not yet conclusive and would require more extensive load studies, e.g., by averaging results from various turbulence realizations [37]. In summary, the PI-LPF$_1$-, PI-LPF$_2$, or I_2-tracking controllers appear to be the best-performing scheme in terms of DEL.

Furthermore, the PBDs of the different control schemes are presented in Table IX. Here, the earlier hypothesis is confirmed. The highest PBD is found for the I_1-controller, which requires more pitching to track the reference as it does not seem to fully exploit the periodic content already present in the wake. In the PI-LPF$_1$-tracking case, the resulting PBD is slightly higher due to more extensive pitch variations and impacts the fatigue life of the bearing more than the other remaining cases. The I_2 controller exhibits the lowest PBD, as it is the least aggressive controller. The reason for a high PBD for the PI-LPF$_1^+$ case is due to the extended $\mathbf{M}_\mathbf{e}^{\text{ref}}$ value, although it is still very reasonable.

Finally, the vertical profile of the mean streamwise velocity in the wake of T2 is analyzed in this section. Fig. 15 showcases these results, where a comparison is made against the baseline case across several rotor diameters behind T2 up to T3 for only the I_1 and PI-LPF$_2$ controller (for clarity's sake). The wake recovery of I_1 appears similar in the first few rotor diameters behind T1 ($x/D = 6$ and $x/D = 7$). However, at $x/D = 10$, PI-LPF$_2$ has much better wake recovery above the hub, translating to the power increase observed at T3 shown in Fig. 14(a).

The PI-LPF$_2$-tracking controller appears superior to the I_1 case, which explains the strong performance gain on T3 compared with the other methods.

VIII. CONCLUSION

This study examined downstream turbine control in a helix wake, proposing two strategies: load rejection and phase synchronization. A novel extension of the multiblade coordinate transformation was proposed, enabling the use of linear PID controllers to execute both strategies. Computational simulations incorporating three turbines demonstrated promising results for the selected cases: load rejection improved turbine fatigue life by up to 10%, while phase synchronization led to a 6% power gain on T3 compared with the baseline helix setup. As inferred in Section VI-C, a more comprehensive turbine fatigue life assessment is beyond the scope of this study and, thus, subject to future work. Further optimization and exploration of advanced control strategies employing this coordinate transformation are recommended, as further power improvements are expected.

ACKNOWLEDGMENT

This work is part of the Hollandse Kust Noord wind farm innovation program where CrossWind C. V., Shell, Grow, Eneco, and Siemens Gamesa are teaming up; funding for the PhDs was provided by CrossWind C. V. and Siemens Gamesa. We further acknowledge the computational resources provided by DelftBlue [35].

REFERENCES

[1] F. González-Longatt, P. Wall, and V. Terzija, "Wake effect in wind farm performance: Steady-state and dynamic behavior," *Renew. Energy*, vol. 39, no. 1, pp. 329–338, Mar. 2012.
[2] R. J. Barthelmie et al., "Modelling and measuring flow and wind turbine wakes in large wind farms offshore," *Wind Energy*, vol. 12, no. 5, pp. 431–444, Jul. 2009.
[3] J. Annoni, P. M. O. Gebraad, A. K. Scholbrock, P. A. Fleming, and J. W. van Wingerden, "Analysis of axial-induction-based wind plant control using an engineering and a high-order wind plant model," *Wind Energy*, vol. 19, no. 6, pp. 1135–1150, Jun. 2016.
[4] D. C. van der Hoek, S. Kanev, J. Allin, D. Bieniek, and N. Mittelmeier, "Effects of axial induction control on wind farm energy production—A field test," *Renew. Energy*, vol. 140, pp. 994–1003, Sep. 2019.
[5] P. A. Fleming et al., "Evaluating techniques for redirecting turbine wakes using SOWFA," *Renew. Energy*, vol. 70, pp. 211–218, Oct. 2014.
[6] J. P. Goit and J. Meyers, "Optimal control of energy extraction in wind-farm boundary layers," *J. Fluid Mech.*, vol. 768, pp. 5–50, Apr. 2015.
[7] J. A. Frederik et al., "Periodic dynamic induction control of wind farms: Proving the potential in simulations and wind tunnel experiments," *Wind Energy Sci.*, vol. 5, no. 1, pp. 245–257, Feb. 2020.
[8] J. A. Frederik and J. W. van Wingerden, "On the load impact of dynamic wind farm wake mixing strategies," *Renew. Energy*, vol. 194, pp. 582–595, Jul. 2022.
[9] J. A. Frederik, B. M. Doekemeijer, S. P. Mulders, and J. W. van Wingerden, "The helix approach: Using dynamic individual pitch control to enhance wake mixing in wind farms," *Wind Energy*, vol. 23, no. 8, pp. 1739–1751, Aug. 2020.

[10] E. Taschner, A. A. W. van Vondelen, R. Verzijlbergh, and J. W. van Wingerden, "On the performance of the helix wind farm control approach in the conventionally neutral atmospheric boundary layer," *J. Phys., Conf. Ser.*, vol. 2505, no. 1, May 2023, Art. no. 012006.
[11] D. C. van der Hoek, B. Van den Abbeele, C. S. Ferreira, and J. W. van Wingerden, "Maximizing wind farm power output with the helix approach—Experimental validation and wake analysis using tomographic PIV," 2023, *arXiv:2306.12849*.
[12] L. J. Huang, S. P. Mulders, E. Taschner, and J. W. van Wingerden, "Enhancing wake mixing in wind farms by multi-sine signals in the helix approach," in *Proc. Amer. Control Conf. (ACC)*, May 2023, pp. 824–830.
[13] H. Korb, H. Asmuth, and S. Ivanell, "The characteristics of helically deflected wind turbine wakes," *J. Fluid Mech.*, vol. 965, p. 2, Jun. 2023.
[14] A. A. W. van Vondelen, J. Ottenheym, A. K. Pamososuryo, S. T. Navalkar, and J. W. van Wingerden, "Phase synchronization for helix enhanced wake mixing in downstream wind turbines," *IFAC-PapersOnLine*, vol. 56, no. 2, pp. 8426–8431, 2023.
[15] E. A. Bossanyi, "Individual blade pitch control for load reduction," *Wind Energy, Int. J. Prog. Appl. Wind Power Convers. Technol.*, vol. 6, no. 2, pp. 119–128, Apr. 2003.
[16] A. V. Oppenheim, A. S. Willsky, S. H. Nawab, and J.-J. Ding, *Signals and Systems*, vol. 2. Upper Saddle River, NJ, USA: Prentice-Hall, 1997.
[17] E. van Solingen and J. W. van Wingerden, "Linear individual pitch control design for two-bladed wind turbines," *Wind Energy*, vol. 18, no. 4, pp. 677–697, Apr. 2015.
[18] S. P. Mulders, A. K. Pamososuryo, G. E. Disario, and J. W. van Wingerden, "Analysis and optimal individual pitch control decoupling by inclusion of an azimuth offset in the multiblade coordinate transformation," *Wind Energy*, vol. 22, no. 3, pp. 341–359, Mar. 2019.
[19] A. K. Pamososuryo, S. P. Mulders, R. Ferrari, and J. W. van Wingerden, "On the analysis and synthesis of wind turbine side-side tower load control via demodulation," 2023, *arXiv:2309.01633*.
[20] A. A. W. Van Vondelen, S. T. Navalkar, D. R. H. Kerssemakers, and J. W. Van Wingerden, "Enhanced wake mixing in wind farms using the helix approach: A loads sensitivity study," in *Proc. Amer. Control Conf. (ACC)*, May 2023, pp. 831–836.
[21] G. Van der Veen, J. W. van Wingerden, M. Bergamasco, M. Lovera, and M. Verhaegen, "Closed-loop subspace identification methods: An overview," *IET Control Theory Appl.*, vol. 7, no. 10, pp. 1339–1358, 2013.
[22] A. A. W. van Vondelen, A. K. Pamososuryo, S. T. Navalkar, and J. W. van Wingerden, "On the optimal azimuth offset for individual pitch control in aeroelastic code coupled with a high-fidelity flow solver," in *Proc. Eur. Control Conf. (ECC)*, Jun. 2024, pp. 2411–2416.
[23] B. Jonkman et al., "OpenFAST/openfast: OpenFAST v3.4.0," Zenodo, Version V3.4.0, Jan. 2023, doi: 10.5281/zenodo.7527379.
[24] E. Gaertner et al., "IEA wind TCP task 37: Definition of the IEA 15-megawatt offshore reference wind turbine," Nat. Renew. Energy Lab. (NREL), Golden, GO, USA, Tech. Rep. NREL/TP-5000-75698, 2020.
[25] N. J. Abbas et al., "NREL/ROSCO: RAAW v1.2," Zenodo, Version raaw1.2, May 2022, doi: 10.5281/zenodo.6543598.
[26] J. N. Sørensen and W. Z. Shen, "Numerical modeling of wind turbine wakes," *J. Fluids Eng.*, vol. 124, no. 2, pp. 393–399, Jun. 2002.
[27] M. Brazell, S. Ananthan, G. Vijayakumar, L. Cheung, M. Sprague, ExaWind Exascale Computing Project Team, and High Fidelity Modeling Project Team, "Amr-wind: Adaptive mesh-refinement for atmospheric-boundary-layer wind energy simulations," in *Proc. APS Division Fluid Dyn. Meeting Abstr.*, Jan. 2021, Paper T29.007. [Online]. Available: https://ui.adsabs.harvard.edu/abs/2021APS..DFDT29007B
[28] L. Cheung, M. J. Brazell, A. Hsieh, S. Ananthan, G. Vijayakumar, and N. deVelder, "Computation and comparison of the stable northeastern U.S. marine boundary layer," in *Proc. AIAA Scitech Forum*, Jan. 2021, p. 454.
[29] D. Allaerts and J. Meyers, "Large eddy simulation of a large wind-turbine array in a conventionally neutral atmospheric boundary layer," *Phys. Fluids*, vol. 27, no. 6, Jun. 2015, Art. no. 065108.
[30] P. K. Taylor and M. J. Yelland, "The dependence of sea surface roughness on the height and steepness of the waves," *J. Phys. Oceanogr.*, vol. 31, no. 2, pp. 572–590, Feb. 2001.
[31] H. Wurps, G. Steinfeld, and S. Heinz, "Grid-resolution requirements for large-eddy simulations of the atmospheric boundary layer," *Boundary-Layer Meteorol.*, vol. 175, no. 2, pp. 179–201, May 2020.
[32] S. Zilitinkevich, I. Esau, and A. Baklanov, "Further comments on the equilibrium height of neutral and stable planetary boundary layers," *Quart. J. Roy. Meteorolog. Soc.*, vol. 133, no. 622, pp. 265–271, Jan. 2007.
[33] *Crosswind Hollandse Kust Noord*. Accessed: Jul. 15, 2024. [Online]. Available: https://www.crosswindhkn.nl/windfarm
[34] J.-A. Dahlberg, "Assessment of the Lillgrund windfarm, power performance and wake effects. Lillgrund pilot project," Swedish Energy Agency, Sweden, Tech. Rep. NEI-SE-865, 2009.
[35] Delft High Perform. Comput. Centre (DHPC). (2022). *DelftBlue Supercomputer (Phase 1)*. [Online]. Available: https://www.tudelft.nl/dhpc/ark:/44463/DelftBluePhase1
[36] S. Skogestad and I. Postlethwaite, *Multivariable Feedback Control: Analysis and Design*. Hoboken, NJ, USA: Wiley, 2005.
[37] *Wind Energy Generation System—Part 1*, IEC Standard 61400-3: 2019, Int. Electrotechnical Commission, Geneva, Switzerland, 2019.
[38] D. Kerssemakers, "On the load impact of the helix approach on offshore wind turbines: Quantifying and analyzing the fatigue load impact of the helix approach on offshore wind turbine components," Master thesis, Delft Univ. Technol., Delft, The Netherlands, 2022.

Aemilius A. W. van Vondelen was born in Zeist, The Netherlands, in 1997. He received the B.Sc. degree in mechanical engineering and the M.Sc. degree in systems and control from the Delft University of Technology, Delft, The Netherlands, in 2017 and 2021, respectively, where he is currently pursuing the Ph.D. degree.

His research interests include the development of innovative pitch control solutions for wind turbines and wind farms that balance loads and power gains, where he collaborates closely with the industry.

Atindriyo K. Pamososuryo was born in Medan, Indonesia, in 1991. He received the M.Sc. and Ph.D. degrees from the Delft Center for Systems and Control, Delft University of Technology, Delft, The Netherlands, in 2018 and 2024, respectively.

In particular, his main focus is on wind energy field applications, where he also collaborated with Vestas Wind Systems A/S, IJmuiden, The Netherlands. His research interests include dynamical system modeling, state estimation, linear parameter-varying systems, and model predictive control.

Dr. Pamososuryo received the O. Howard Schuck Award from the American Automatic Control Council for his contribution to the applied control engineering field in 2023.

Sachin T. Navalkar was born in Mumbai, India, in 1986. He received the M.Sc. degree in control engineering and the Ph.D. degree in sustainable energy from the Delft University of Technology, Delft, The Netherlands, in 2009 and 2016, respectively. His Ph.D. thesis was on iterative data-driven control for flexible wind turbine rotors.

He is currently an Advisory Engineer with Siemens Gamesa Renewable Energy, The Hague, The Netherlands. His research interests include the technology area of load assessment, optimization, and design solutions for wind turbine support structures.

Jan-Willem van Wingerden (Senior Member, IEEE) was born in Ridderkerk, The Netherlands, in 1980. He received the B.S. degree in mechanical engineering and the Ph.D. degree (cum laude) in control engineering from the Delft Center for Systems and Control, Delft University of Technology, Delft, The Netherlands, in 2004 and 2008, respectively. His Ph.D. thesis was on smart dynamic rotor control for large offshore wind turbines.

He is currently a full Professor with the Delft University of Technology. His current research interests include the development of data-driven controllers for wind turbines and wind farms.